SCIENTIFIC REPORTS

OPEN

SUBJECT AREAS:
COMPOSITES
STRUCTURAL PROPERTIES
SURFACES, INTERFACES AND THIN FILMS
ATOMISTIC MODELS

Received
14 February 2014

Accepted
7 March 2014

Published
27 March 2014

Correspondence and requests for materials should be addressed to X.-Y.L. (xyliu@lanl.gov)

Revisiting the Al/Al_2O_3 Interface: Coherent Interfaces and Misfit Accommodation

Ghanshyam Pilania[1], Barend J. Thijsse[2], Richard G. Hoagland[1], Ivan Lazić[2], Steven M. Valone[1] & Xiang-Yang Liu[1]

[1]Materials Science and Technology Devision, Los Alamos National Laboratory, Los Alamos, New Mexico 87545, USA and,
[2]Department of Materials Science and Engineering, Delft University of Technology, Mekelweg 2, 2628 Delft, The Netherlands.

We study the coherent and semi-coherent Al/α-Al_2O_3 interfaces using molecular dynamics simulations with a mixed, metallic-ionic atomistic model. For the coherent interfaces, both Al-terminated and O-terminated nonstoichiometric interfaces have been studied and their relative stability has been established. To understand the misfit accommodation at the semi-coherent interface, a 1-dimensional (1D) misfit dislocation model and a 2-dimensional (2D) dislocation network model have been studied. For the latter case, our analysis reveals an interface dislocation structure with a network of three sets of parallel dislocations, each with pure-edge character, giving rise to a pattern of coherent and stacking-fault-like regions at the interface. Structural relaxation at elevated temperatures leads to a further change of the dislocation pattern, which can be understood in terms of a competition between the stacking fault energy and the dislocation interaction energy at the interface. Our results are expected to serve as an input for the subsequent dislocation dynamics models to understand and predict the macroscopic mechanical behavior of Al/α-Al_2O_3 composite heterostructures.

Aluminum is one of the world's most widely used metals, in large part due to its superior strength-to-weight ratio, while alumina (Al_2O_3) is one of the most strongly bonded compounds in existence (with enthalpy of formation of 1674.4 kJ/mol)[1,2] and is widely used as a catalyst support, for structural ceramics, and as a substrate for film growth[3–6] Among the various polymorphs of alumina, corundum (α-Al_2O_3) is the most stable phase at the ambient conditions and has been extensively studied[7] The Al/α-Al_2O_3 interface is of enormous scientific and technological significance due to the crucial role it plays in a range of important applications such as metal-ceramic composites, protective coating for Al, casting and smelting processes, microelectronics, corrosion/wear protection and catalysis[8–11] As a consequence, large amount of experimental[8,12–22] and theoretical[23–33] research work has been devoted to this interface.

Based on high-resolution transmission electron microscopy, the primary orientational relationship at the Al/α-Al_2O_3 interface has been observed to be one that matches the close-packed planes and directions in the two phases[17] In this orientation the Al(111) plane is parallel to the Al_2O_3(0001) basal plane and the following directions are parallel to each other:

$$\langle \bar{1}01\rangle_{Al} \| \langle 01\bar{1}0\rangle_{Al_2O_3} \tag{1}$$

$$\langle \bar{1}2\bar{1}\rangle_{Al} \| \langle 2\bar{1}\bar{1}0\rangle_{Al_2O_3} \tag{2}$$

As is the case for other similar metal/Al_2O_3 interfaces[2,34,35], the stoichiometry of clean Al/α-Al_2O_3 interface is a function of the oxygen partial pressure. Previous first principles based analysis[25] has suggested that the clean Al/Al_2O_3 interface can be stoichiometric, oxygen terminated, or aluminum terminated, depending on the ambient oxygen partial pressure. For the relatively low oxygen partial pressures[36], usually associated with sessile drop experiments, the interface is predicted to be stoichiometric. However, for relatively high oxygen partial pressures, prevalent during fracture experiments, the interface has been suggested to be oxygen terminated[25]. Recent experimental[37] and theoretical[31] studies reporting atomically abrupt Al(liquid)/α-Al_2O_3(solid) interface stabilized by self-regulated interfacial Al vacancies have suggested an aluminum terminated interface.

Electronic structure and work of adhesion have been obtained from first principles based quantum mechanical computations by Batyrev and Kleinman[26] and Siegel *et al.*[28,29] assuming a coherent interface. Streitz and Mintmire[32,33,38] employed a force field accounting for the electrostatic interaction associated with charge transfer in their MD simulations to study the solid Al/Al_2O_3 interface. However, unlike the experimentally-observed abrupt interface[17], the force field predicted that O atoms should rapidly diffuse into the Al lattice, resulting in a highly disordered region at the interface[33]. Zhang *et al.*[30] have studied the adhesion and nonwetting to wetting transition in the Al/α-Al_2O_3 interface using a reactive force field (ReaxFF) approach[39]. They find that the evaporation of Al atoms and diffusion of O atoms in α-Al_2O_3 primarily lead to the wetting of liquid Al on the oxide surface.

Nanolayered laminated composites of aluminum and aluminum oxide with interlayer spacing ranging from 50 to 500 nm have been prepared in the past[40] and found to exhibit interesting deformation mechanism with extensive ductility. However, an atomistic understanding of the observed mechanical behavior is presently lacking. Although available dislocation dynamics models are capable of exploring evolution of interface dislocation networks and can predict the microscopic properties of the nanolayered composites during mechanical deformations at large length scales, such models depend upon atomistic input to define interfacial properties and dislocation reaction rules. A deeper understanding of the interface structure can be crucial for understanding the macroscopic mechanical behavior of the nanolayered composite heterostructures.

However, despite the significance of interfacial structure, studies addressing them have remained quite scarce in the literature. The reason for this scarcity is two fold. On the one hand, accurate *ab initio* simulation techniques are not efficient enough to practically deal with such large systems with several thousand systems[41]. On the other hand, sophisticated atomistic potentials required for molecular dynamics (MD) simulations, that can treat both metal and ceramic systems on equal footing and adequately describe charge transfer effects at the interface, were unavailable until recently. As a first step towards this direction, the goal of the present study is to elucidate the coherent and semi-coherent interface structures at the Al(111)/α-Al_2O_3(0001) interface. This work is expected to provide novel information on dislocation patterns that can form at the interface to accommodate misfit strain as well as on the factors that govern the formation of these patterns. The resulting knowledge from the present study is expected to serve as an input for the subsequent dislocation dynamics models[42,43] to understand and predict the macroscopic mechanical behavior of Al/α-Al_2O_3 composite heterostructures.

Results

Coherent Interfaces. Employing the aforementioned experimentally observed orientational relationship[17], the Al/α-Al_2O_3 interface was modeled in a slab geometry periodically repeating in the plane of the interface. Further details of the aomistic model used and the computational methodology employed can be found in the Methods section presented towards the end of the manuscript. To start with, both the O-terminated and the Al-terminated interfaces were considered in our atomistic simulations. Since our computed lattice constant for the fcc-Al (a_{Al} = 4.05 Å) and the α-alumina ($a_{\mathrm{Al_2O_3}} = 4.762$ Å and $c_{\mathrm{Al_2O_3}} = 12.99$ Å) are in excellent agreement with the corresponding experimentally measured[17] values, we recover the correct magnitude of the measured misfit strain

$$\delta = 2\,\frac{\sqrt{3/2}a_{\mathrm{Al}} - a_{\mathrm{Al_2O_3}}}{\sqrt{3/2}a_{\mathrm{Al}} + a_{\mathrm{Al_2O_3}}} = 0.041. \tag{3}$$

The crystal geometry in the 2D interface is as follows. The periodic lengths in the parallel directions $[\bar{1}01]_{\mathrm{Al}}$ and $[01\bar{1}0]_{\mathrm{Al_2O_3}}$ are $a_{\mathrm{Al}}\big/\sqrt{2}$ and $\sqrt{2}a_{\mathrm{Al_2O_3}}$ in the aluminum and alumina crystals, respectively. On the other hand, the periodic lengths in the directions $[\bar{1}2\bar{1}]_{\mathrm{Al}}$ and $[2\bar{1}\bar{1}0]_{\mathrm{Al_2O_3}}$ are $\sqrt{\frac{3}{2}}a_{\mathrm{Al}}$ and $a_{\mathrm{Al_2O_3}}$ in the aluminum and alumina crystals, respectively. For a coherent interface three periods in aluminum match one period in alumina along the direction $[\bar{1}01]_{\mathrm{Al}} \| [01\bar{1}0]_{\mathrm{Al_2O_3}}$, while one period in aluminum matches one period in alumina along the normal direction (*i.e.*, $[\bar{1}2\bar{1}]_{\mathrm{Al}} \| [2\bar{1}\bar{1}0]_{\mathrm{Al_2O_3}}$). As shown in Eq. (3), this produces a compressive strain of 0.041 in both the directions on the aluminum.

Figure 1(a) shows our fully relaxed interfacial geometry between the Al (111) and the O-terminated α-Al_2O_3 (0001) at 0 K. We find that the computed interface geometry agrees well with the one obtained using first principles density functional theory based calculations[27] carried out using generalized gradient approximation of Perdew *et al.*[44] We further note that the atomic arrangement in the vicinity of the interface plane is strongly influenced by the α-Al_2O_3 structure and leads to a splitting of the Al metal layer closest to the interface into three distinct sub-layers (namely, layers A_1, A_2 and A_3, as marked in Fig. 1(a)) after relaxation. The Al atoms in the first two sublayers (*i.e.*, the layers A_1 and A_2) occupy the sites that are dictated by a natural continuation of the α-Al_2O_3 lattice. That is, the Al metal atoms in the first two sub-layers are pulled toward the O-terminated alumina surface, occupying the sites that Al would occupy in

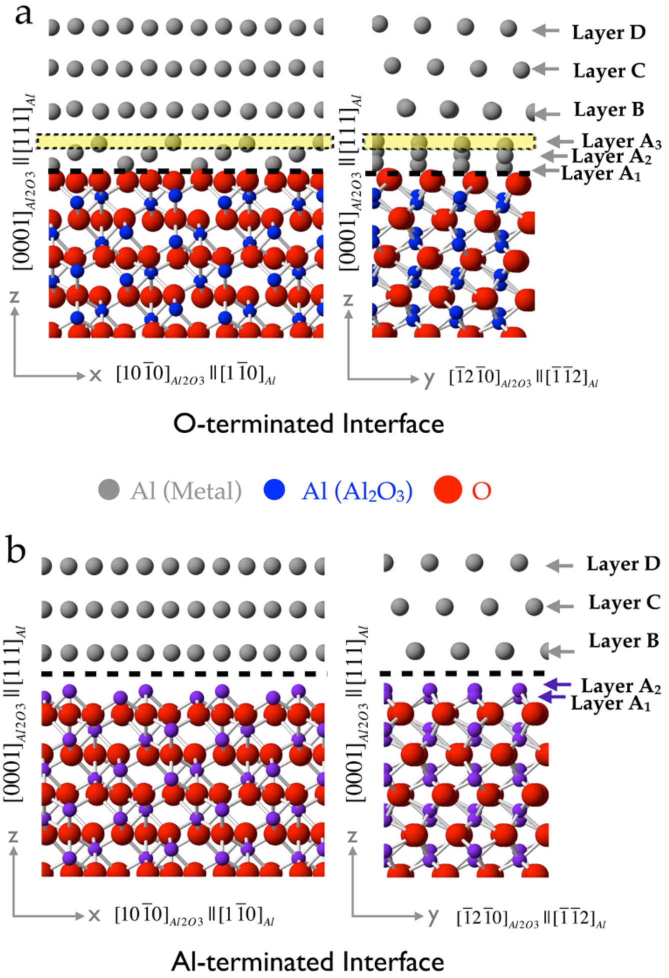
a
Layer D
Layer C
Layer B
Layer A_3
Layer A_2
Layer A_1
$[0001]_{Al2O3} \| [111]_{Al}$
z
x $[10\bar{1}0]_{Al2O3} \| [1\bar{1}0]_{Al}$
y $[\bar{1}2\bar{1}0]_{Al2O3} \| [\bar{1}\bar{1}2]_{Al}$
O-terminated Interface
● Al (Metal) ● Al (Al_2O_3) ● O
b
Layer D
Layer C
Layer B
Layer A_2
Layer A_1
$[0001]_{Al2O3} \| [111]_{Al}$
z
x $[10\bar{1}0]_{Al2O3} \| [1\bar{1}0]_{Al}$
y $[\bar{1}2\bar{1}0]_{Al2O3} \| [\bar{1}\bar{1}2]_{Al}$
Al-terminated Interface

Figure 1 | Coherent interface models. Schematic of Front (left) and side (right) views of the relaxed structure of (a) O-terminated and (b) Al-terminated coherent Al/α-Al_2O_3 interfaces. For clarity Al atoms on the metal side of the interface have been distinguished (colored differently) than that of the Al_2O_3 side.

bulk alumina. By relaxing in this way, all the dangling bonds on the oxygen ions at the interface are saturated. The Al atoms in the third sub-layer (*i.e.*, the layer A_3), are not directly bonded to the interfacial O atoms and occupy a hollow site in a slightly distorted hexagonal lattice formed by the first two Al metal sub-layers.

The relaxed interface geometry between the Al (111) and the Al-terminated α-Al_2O_3 (0001) interface is presented in Fig. 1(b). In their first principles investigation, Zhang *et al.*[25] have found this surface configuration as the most stable after considering a number of interface configurations of Al atoms in the metal layer adjacent to the interface with respect to the alumina surface, reached by effectively sliding the metal layer along the alumina surface. It is interesting to note here that the Al-terminated interface shown in Fig. 1(b) can be formed by removing the third sub-layer A_3 (highlighted in Fig. 1(a)) of the Al metal atoms in the O-terminated interface. Therefore, the chemical potential of the Al atoms in the layer A_3 can be used to evaluate the relative stability of the two interfaces. We find that the transfer of the Al atoms in the the layer A_3 of the O-terminated interface to a bulk Al metal reservoir is indeed thermodynamically favorable, resulting in the lower-energy Al-terminated interface. This indicates the superior stability of the Al-terminated interface in a low oxygen chemical potential regime. According to our CTIP+RFMEAM potential calculations the Al-terminated interface is more stable by 1.98 J/m^2, while parallel DFT-PBE calculations also show a qualitative agreement favoring the Al-termination by 0.90 J/m^2 over the O-termination.

Based on interface adhesion energy analysis, previous DFT calculations have also predicted the Al-termination for the Al(111)/α-Al_2O_3 solid-solid interfaces[28]. We also note that Al(liquid)/α-Al_2O_3(solid) interface has also recently been found to be atomistically sharp with Al termination in both *in situ* high-resolution transmission electron microscopy experiments[37] as well as through first-principles MD simulations[31]. Therefore, we chose the Al-terminated interface to study the structure of misfit dislocations at this interface. However, we do not expect the pattern of misfit dislocations formed at the O-terminated interface to be drastically different than that of the Al-terminated interface, since the two interfaces are related to one another through addition or removal of an extra sub-layer of Al atoms in the vicinity of the interface plane. Such mass transport should be easily achievable by a suitable mechanism such as dislocation glide or diffusion of Al atoms on the metal side of the interface, especially at elevated temperatures.

1D Misfit Dislocations. Since the lattice parameters in the Al and the α-Al_2O_3 phases are not identical, a long range elastic stress field accompanies a perfectly coherent interface. The coherency field can be relieved through formation of a 2D misfit dislocation network at the interface. However, before going to the case of a 2D network, we first investigate the case of misfit dislocation arrays only along the $[\bar{1}01]_{Al}||[01\bar{1}0]_{Al_2O_3}$ direction, while assuming a perfectly coherent interface along the $[\bar{1}2\bar{1}]_{Al}||[2\bar{1}\bar{1}0]_{Al_2O_3}$ direction. For this 1D misfit model, the interface supercell dimensions along the directions $[\bar{1}01]_{Al}||[01\bar{1}0]_{Al_2O_3}$ and $[\bar{1}2\bar{1}]_{Al}||[2\bar{1}\bar{1}0]_{Al_2O_3}$ were 65.96 Å and 4.76 Å, respectively. In this case, to minimize overall strain in the $[\bar{1}01]_{Al}$ direction, twenty-three aluminum periods were made to match eight alumina periods, instead of the 3 : 1 ratio that produces a coherent interface. This reduces the overall strain in this direction from 0.041 to 1.78×10^{-3}. In the other direction the period ratio was kept at 1 : 1, leaving the strain unaltered at 0.041, as mentioned above for a perfectly coherent interface.

To quantify the misfit dislocation structure, we measured disregistry across the interface plane after relaxation. For the disregistry measurement the two Al layers nearest to the relaxed interface plane (one on Al_2O_3 side and one on the Al metal side) were taken into account (*c.f.* Fig. 2(a)). To carryout this measurement a reference state must be chosen, in which the two adjoining crystals are coherent. To construct the coherent dichromatic pattern (CDP) reference state[45], we compressed and stretched the Al layers on the Al-metal side and on the Al_2O_3 side, respectively, by equal amounts along the direction $[\bar{1}01]_{Al}||[01\bar{1}0]_{Al_2O_3}$. The top and side views of the reference state are depicted in Fig. 2(b). After constructing the reference state, a correspondence list between nearest neighbor Al atoms in the metal layer and the ceramic layer is compiled in this configuration. Disregistry vectors $\Delta\vec{r}$ are finally computed as

$$\Delta\vec{r} = \vec{r}_{ij}^{D} - \vec{r}_{ij}^{R}, \qquad (4)$$

where $\vec{r}_{ij}^{R}$ is the relative position between the i^{th} atom and the j^{th} atom that form a pair in the reference and $\vec{r}_{ij}^{D}$ is the relative position

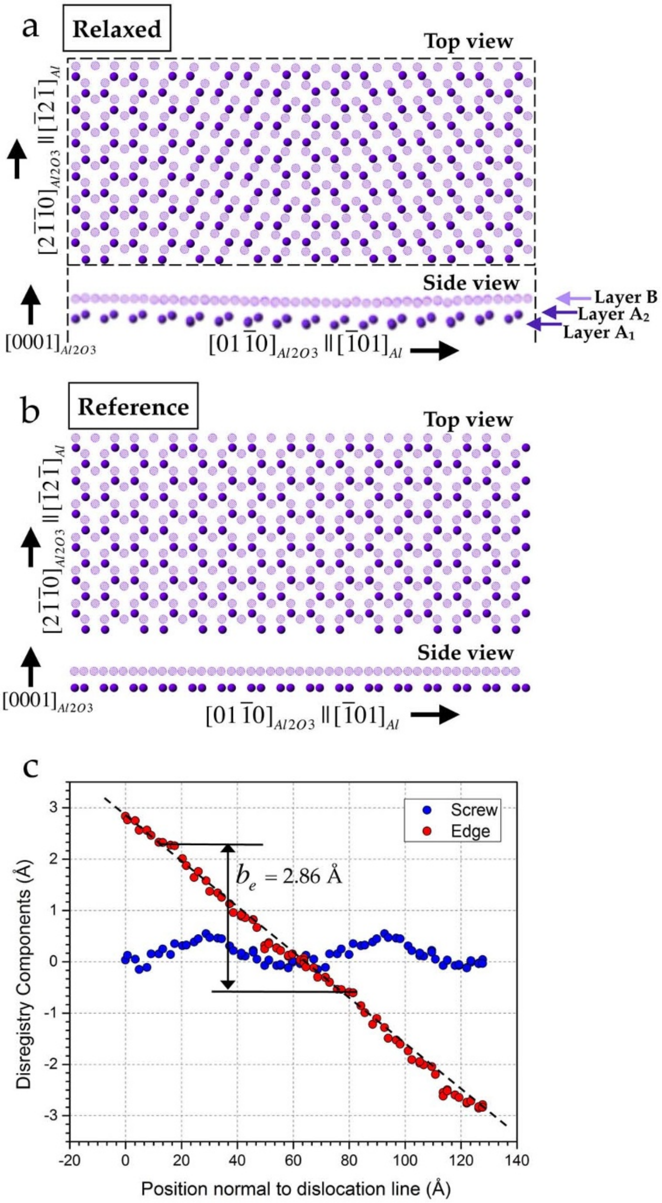

Figure 2 | 1D misfit dislocation model. (a) Relaxed and (b) coherent dichromatic pattern (CDP) reference structures containing two Al layers nearest to the interface that were used for the disregistry analysis of the 1D misfit dislocation model. Al atoms on the ceramic and metal sides of the interface have been shown in purple and lavender colors, respectively. (c) Disregistry vectors $\Delta\vec{r}$ computed as the difference between the positions of the selected pair of Al atoms in the relaxed and reference configurations. (d) Screw and edge components of the disregistry vectors.

between the same pair of atoms at the interface[46,47]. The disregistry between the two Al atomic planes on either side of the interface is thus a position dependent vector field. Furthermore, since the Burgers vectors of the misfit dislocation arrays are expected to lie within the interface plane, we restrict our attention to disregistry components along the directions $[\bar{1}01]_{\mathrm{Al}}$ and $[\bar{1}2\bar{1}]_{\mathrm{Al}}$ only. We find that the resulting disregistry pattern is mainly dominated by the homogeneous deformation used in constructing the strained reference configuration. As a further analysis, in Fig. 2(d) we plot the components $\Delta\vec{r}\cdot\hat{\xi}$ and $\Delta\vec{r}\cdot\hat{n}$ of the disregistry vectors along directions $\hat{\xi}$ and $\hat{n}$, parallel and normal to the set of misfit dislocation lines (laying along the direction $[\bar{1}2\bar{1}]_{\mathrm{Al}}$), respectively. We find that the screw component along the direction $\hat{\xi}$ remains close to zero throughout and exhibits some small deviations owing to a slight buckling of the Al metal layer adjacent to the interface plane after relaxation. On the other hand, the edge component along the direction $\hat{n}$ simply shows a straight line with a constant slope. The shape of this pattern is indicative of the presence of a purely Vernier-type misfit dislocation with wide overlapping dislocation cores.

2D Misfit Dislocation Network. For the 2D misfit dislocation model, the dimension of the supercell along the directions $[\bar{1}01]_{\mathrm{Al}} \| [01\bar{1}0]_{\mathrm{Al_2O_3}}$ and $[\bar{1}2\bar{1}]_{\mathrm{Al}} \| [2\bar{1}\bar{1}0]_{\mathrm{Al_2O_3}}$ were 65.96 Å and 114.29 Å, respectively. Here, twenty-three aluminum periods were made to match eight alumina periods in the $[\bar{1}01]_{\mathrm{Al}}$ direction and twenty-three aluminum periods were made to match twenty-four alumina periods in the $[\bar{1}2\bar{1}]_{\mathrm{Al}}$ direction. The dimensions of the simulation cell were chosen so as to minimize the strain required for maintaining the periodic boundary conditions along the two orthogonal sets of directions in the interface plane while maintaining a minimal system size.

After relaxation, the interface structure was analyzed by measuring the disregistry across the interface plane, as described above for the 1D misfit dislocation model. Disregistry vectors $\Delta\vec{r}$ computed as the difference between the positions of the corresponding pair of Al atoms (in the adjacent layers above and below the interface plane) in the relaxed and reference configurations are shown in Fig. 3(a). The edge component $\Delta\vec{r}\cdot\hat{n}$ of the disregistry vectors along the $[\bar{1}2\bar{1}0]_{\mathrm{Al_2O_3}}$ direction is plotted in Fig. 3(b), while the screw component remains zero throughout and is not shown in the figure. Similar pattern for the disregistry component was also obtained for the $[2\bar{1}\bar{1}0]_{\mathrm{Al_2O_3}}$ and $[\bar{1}\bar{1}20]_{\mathrm{Al_2O_3}}$ directions, indicating that there exist three sets of edge dislocations at an angle of 120° from each other. A closer look at the Fig. 3(b) reveals steps-like flat periodic regions which are the result of the tendency of the interface deformation to localize into compact coherent regions, while the steepest slope correspond to the dislocation cores. Several parameters characterizing the dislocation network can be read from the Fig. 3(b). Difference between successive horizontal flat regions of the disregistry component $\Delta\vec{r}\cdot\hat{n}$ is the magnitude of the net edge component $b_e = 2.48$ Å of the Burgers vectors of the dislocations. On the other hand, the spacing $s = 57.1$ Å between the parallel sets of dislocations along the $[\bar{1}2\bar{1}0]_{\mathrm{Al_2O_3}}$ direction is the distance between the successive horizontal regions along the abscissa.

The 2D dislocation network for the relaxed Al/α-Al_2O_3 interface as predicted from our disregistry analysis is presented in Fig. 3(c). The interface structure reported is also found to be consistent with the Frank–Bilby equation[45,48–50], details of which are provided in the Method section of the present manuscript. For clarity, only three Al-layers (*i.e.*, layer A, consisting both the sub-layers A_1 and A_2, layer B and layer C as depicted in the inset of the Fig. 3(c)) at the interface are included in the figure with atoms in each of the three layers colored according to their charges. The positions and line directions for the identified three sets of edge dislocations are presented as solid black lines and black arrows in the figure, while the Burgers vectors are depicted as blue arrows. The dislocation network clearly reveals coherent (*fcc-like*) and stacking fault (*hcp-like*) regions, separated by the dislocations lines. Some of the coherent (hexagonal) and stacking fault (triangular) regions are highlighted in green and blue, respectively. Here note that, unlike layers B and C, the layer A (*i.e.*, the first Al-layer at the interface on the ceramic side) is not a closed pack layer of Al atoms and has a hexagonal lattice instead. Therefore, the terms *fcc-like* and *hcp-like* are used here only in a qualitative and local sense with their scope limited to the interface region alone.

Figure 4(a) shows the charge distribution of the Al and O atoms across the interface along the $[111]_{\mathrm{Al}} \| [0001]_{\mathrm{Al_2O_3}}$ direction. It can be seen that after a couple of atomic layers away from the interface, on both the metal and the ceramic sides, bulk-like behavior in the charge distribution is recovered. On the metal side the Al atoms remain charge neutral throughout. Surface effects at the free surface on the Al_2O_3 side lead to a deviation in the charges from their respective bulk values. The in-plane charge distribution in the first three Al metal layers closest to the interface is presented in Figures 4b-d. Interestingly, the charges in the first layer B show a charge distribution pattern in close correlation with the coherent regions of the predicted interface structure. This correlation can be attributed to the slight variations in the local coordination of Al atoms influenced by the interface dislocation structure. As we go deeper in the metal side away from the interface, charges quickly diminish in the magnitude and the correlated pattern gradually fades. For instance, the layer C shown in Fig. 4c has an average charge that is about one order of magnitude lower than that of the layer B, nonetheless still shows a pattern in the charge distribution. However, the third metal layer (*i.e.*, the layer D) further away form the interface (*c.f.* Fig. 4(d)) reveals charges that are already negligible as compared to the other two layers and do not carry any correlation with the interface structure.

We note that the interface dislocation structure presented in Fig. 3(c) was obtained at 0 K. In the molecular dynamics run, we started the simulation at 100 K, and systematically removed the kinetic energy of the system in each step during the dynamics. Convergence was reached when the temperature was dropped to 0 K and all the force components on the atoms were lower than 0.01 eV/Å. However, owing to sluggish kinetics at such low temperatures one may not have converged to the thermodynamically most stable state of the system under investigation. To further confirm the anticipated structural change in the interface structure at elevated temperatures, we carried out annealing of the 0 K relaxed structure at 500 K for 200 ps, followed by a ramping down to 0 K over a 100-ps interval and finally relaxation at 0 K for another 200 ps.

The final interface structure is presented in Fig. 5(a) with the three sets of dislocation lines and their Burgers vectors depicted in the figure and is found to be 0.18 J/m^2 lower in energy than the one obtained at 0 K. The structure reveals that the annealing treatment only has an effect of rigidly shifting the relative positions of any of the two parallel sets of dislocations with respect to the third set without changing the relative distance within a given set of dislocations. This leads to an expansion of the alternate triangular *hcp-like* regions (highlighted in blue) around a coherent hexagonal region shown in Fig. 3(c), while the other three regions shrink to form nodes as can be seen highlighted in green in Fig. 5(a). In other words, the *hcp-like* regions transform from equal-area pairs into pairs consisting of a large area triangle and a small area triangular node. Furthermore, the coherent *fcc-like* regions transform into almost triangular shape regions after the annealing treatment. It can also be easily seen that in this interface structure each node is surrounded by alternating *fcc-like* and *hcp-like* regions and has a three-fold symmetry in the interface plane. We note that such interface structures have recently been predicted for interfaces formed between various fcc metals[51].

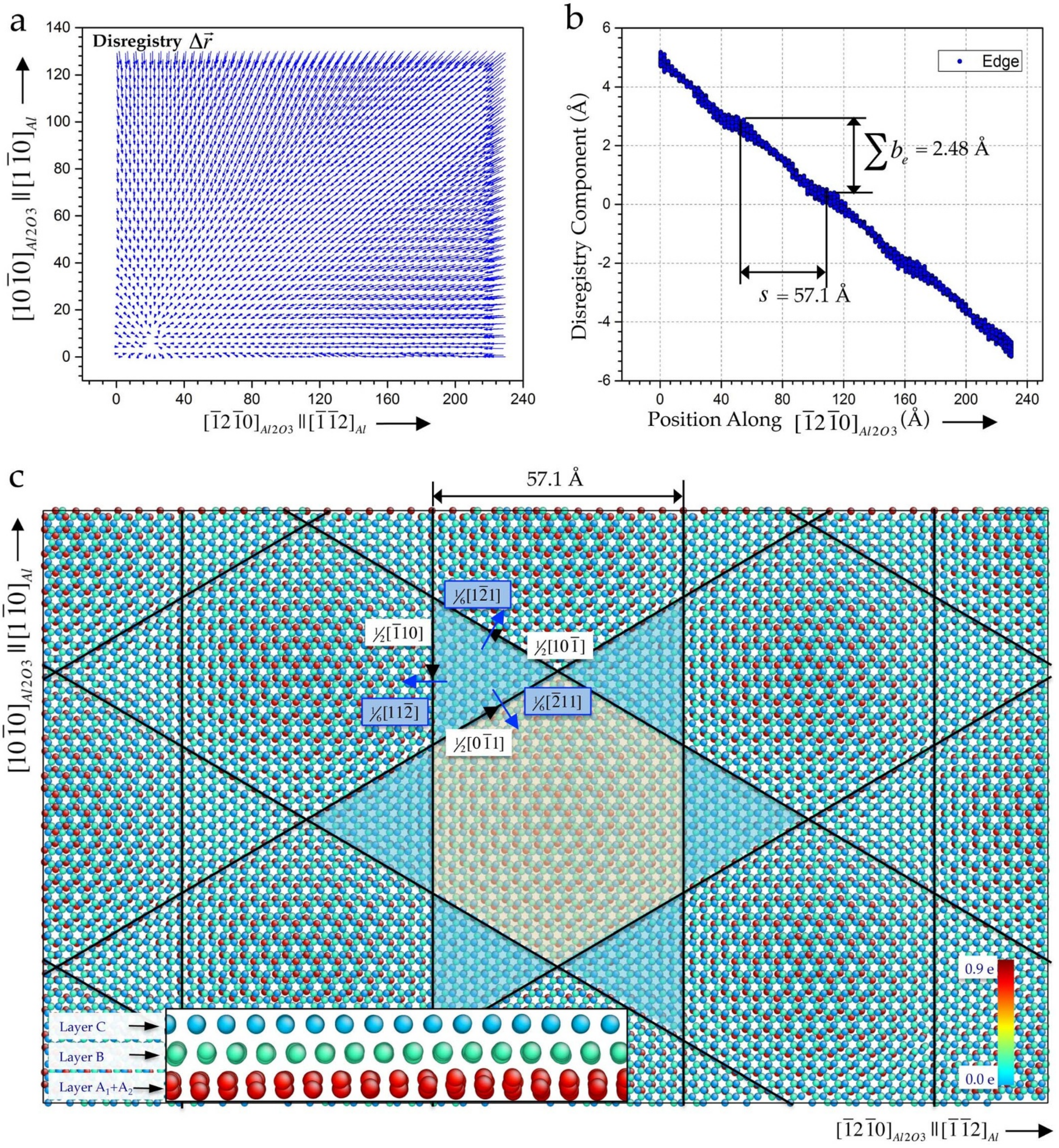

Figure 3 | 2D misfit dislocation network. (a) Disregistry vectors in the interface plane computed with respected to a CDP reference structure. (b) Net edge component of the disregistry vectors along the $[2\bar{1}\bar{1}0]_{Al_2O_3}$ direction. (c) The 2D misfit dislocation network for the relaxed Al/α-Al_2O_3 interface predicted at 0K. Only three Al-layers (namely layers A, B and C as shown in the inset) are included in the figure with atoms in each of the three layers colored according to their charges.

Discussion

To gain a deeper insight into the computed dislocation patterns, next we investigate various factors that might play a role in controlling the predicted interface structure. The energy difference per unit area between the *fcc-like* coherent regions and the *hcp-like* stacking fault regions is one of the crucial factors that has a strong influence on the observed dislocation pattern. In one extreme limit, when the relative energy of the stacking fault regions is much higher than that of the coherent regions, a hexagonal Wigner-Seitz mesh-like network of misfit dislocations around the points of the best matching (indicated as •) in the coherent region is expected[52], as depicted in the top panel of Fig. 6(a).

The other extreme situation arises when the energy difference between the two regions is relatively small, as is the case in the present study. We calculate the difference per unit area between the *hcp-like* stacking fault regions and the *fcc-like* coherent regions to be

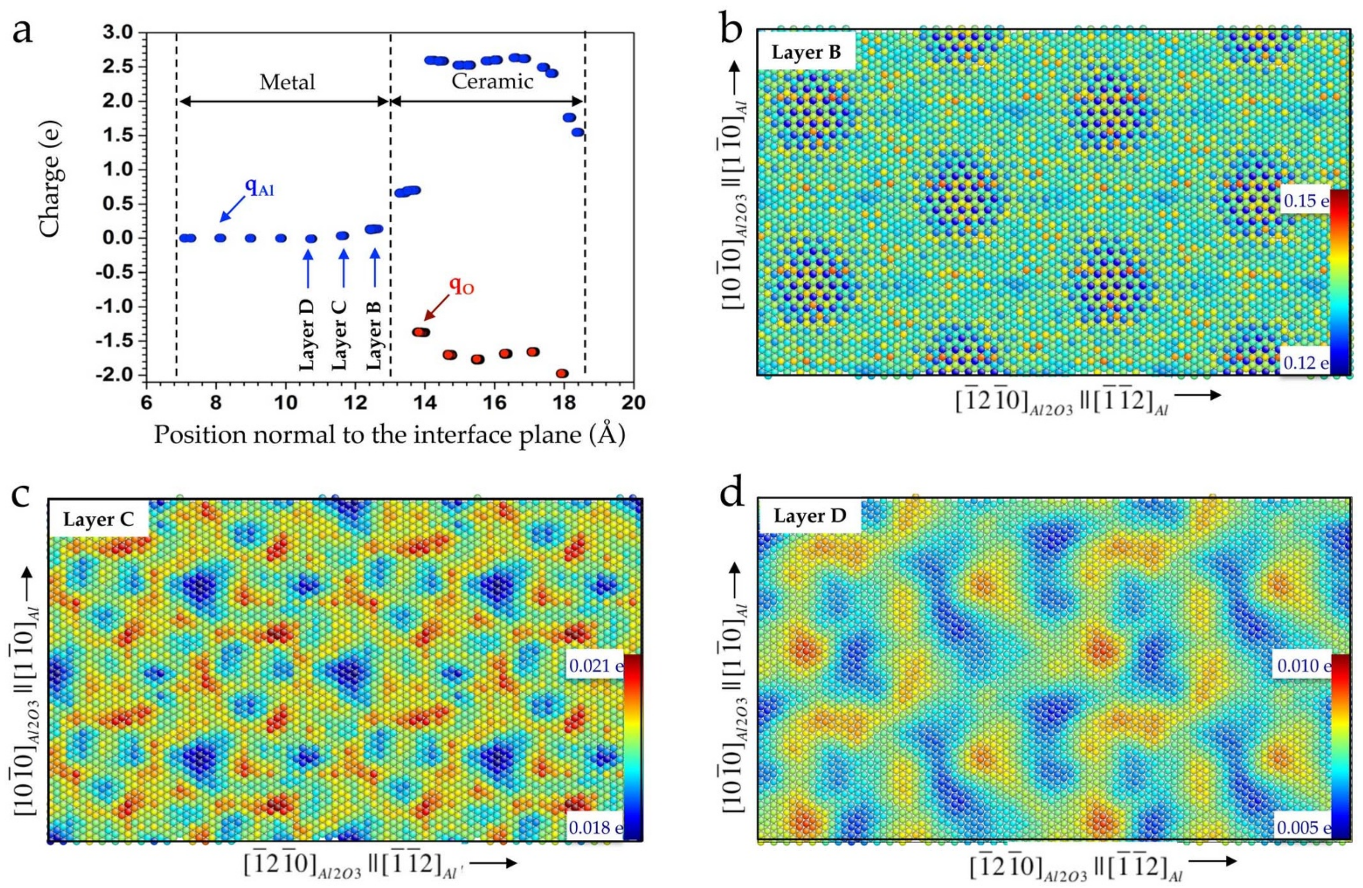

Figure 4 | Charge distributions. (a) The charge distribution profile of the Al and O atoms normal to the interface plane along the $[111]_{Al}||[0001]_{Al_2O_3}$ direction for the 2D misfit dislocation network relaxed at 0K. The in-plane charge distribution in the (b) first, (c) second and (d) third Al layers closest to the interface on the metal side.

0.03 J/m^2 (compared to our DFT computed value of 0.08 J/m^2). In this case, the alternate nodes in the hexagonal Wigner-Seitz mesh-like network of misfit dislocations (shown as ⊕ in the top panel of Fig. 6(a)) grow at the expense of the coherent regions until the ratio of their interfacial areas approaches unity. As a result, a triangular mesh of Shockley partial dislocations, as shown in the bottom panel of Fig. 6(a), is observed. Note that going from one extreme case of the hexagonal mesh to the other extreme case of the triangular mesh, the

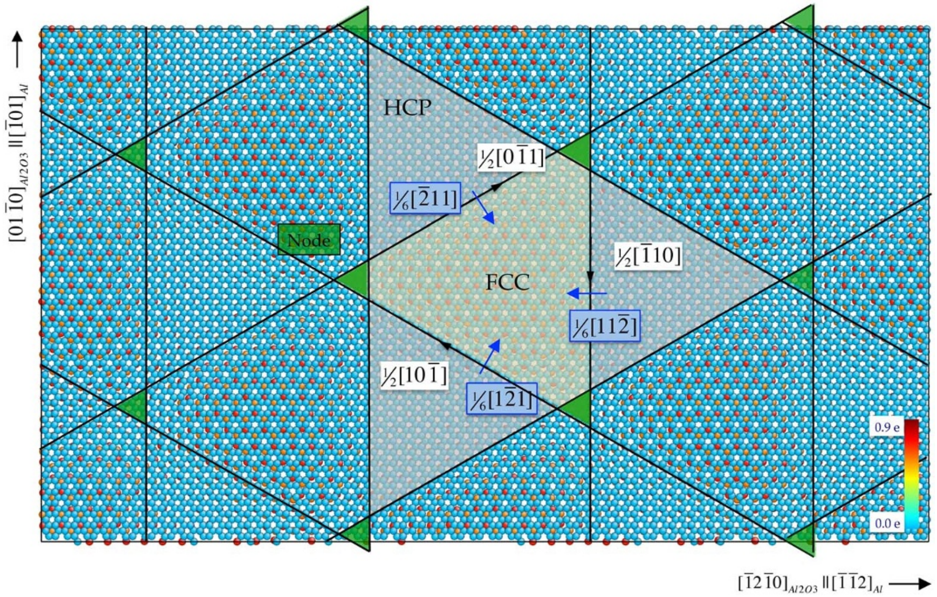
HCP
FCC
Node
$\frac{1}{2}[0\bar{1}1]$
$\frac{1}{6}[\bar{2}11]$
$\frac{1}{2}[\bar{1}10]$
$\frac{1}{6}[11\bar{2}]$
$\frac{1}{2}[10\bar{1}]$
$\frac{1}{6}[12\bar{1}]$
0.9 e
0.0 e
$[01\bar{1}0]_{Al2O3} \parallel [\bar{1}01]_{Al}$
$[\bar{1}2\bar{1}0]_{Al2O3} \parallel [\bar{1}\bar{1}2]_{Al}$

Figure 5 | 2D misfit dislocation network after annealing. The 2D misfit dislocation network for the relaxed Al/α-Al_2O_3 interface after annealing at 500 K. For clarity, only three Al-layers depicted in Fig. 3(c) are shown with atoms in each of the three layers colored according to their charges.

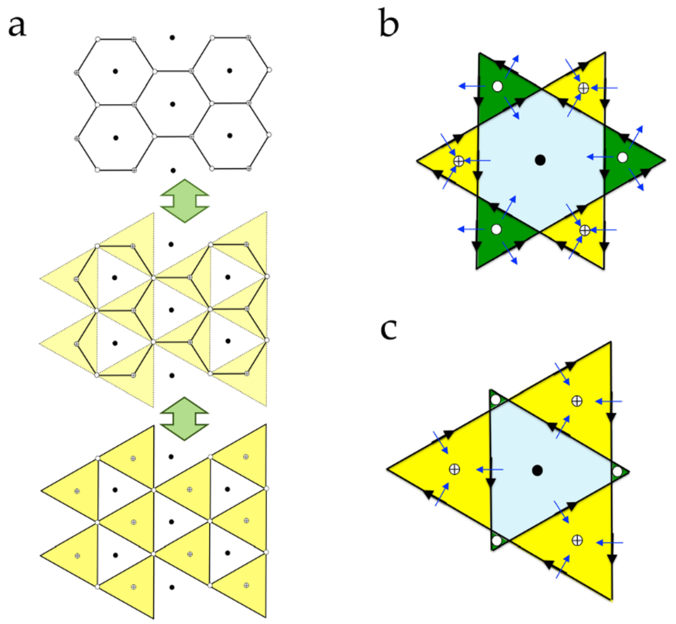

Figure 6 | Dislocation network patterns at the Al-Al$_2$O$_3$ interface. (a) Schematic illustration depicting the effect of the relative energy difference per unit area between the *fcc-like* coherent regions and the *hcp-like* stacking fault regions at the interface. A high stacking fault energy favors a hexagonal network of dislocations, while a low stacking fault energy leads to a triangular dislocation mesh. (b) and (c) represent the schematics of the dislocation patterns obtained in the present study at 0 K and after annealing at 500 K, respectively. The dislocation line directions and Burgers vectors are shown by black and blue arrows, respectively. See text for further details.

area ratio of the stacking fault regions to the coherent regions varies from zero to one. The two interface dislocation patterns, reported in Fig. 3(c) and Fig. 5, that we have predicted here represent two intermediate situations between the two possible extreme cases with the ratio of the two regions being $\frac{1}{3}$ and slightly lower than 1 and are depicted schematically in Fig. 6(b) and Fig. 6(c), respectively.

Dislocation interaction is the second important factor that controls the observed dislocation pattern at the interface. To further elucidate this factor, in Fig. 6(b) we have schematically captured the dislocation pattern obtained through structural relaxation near the absolute temperature. The dislocation lines and Burgers vector directions are shown by black and blue arrows, respectively. The center of the coherent region is marked by symbol •, while the symbols ○ and ⊕ mark the centers of the alternate triangular stacking fault regions. It is interesting to note that the dislocation interactions are attractive and repulsive in the alternate triangular regions colored in green and yellow, respectively, in Fig. 6(b). Therefore, owing to the attractive interactions, a high temperature relaxation leads the green triangular regions to shrink and collapse in a node. On the other hand, the yellow triangles belonging to the second set of the stacking fault regions, shown in Fig 6(b), grow larger upon relaxation to push the dislocations further apart in order to minimize their repulsive interactions. This leads to the dislocation pattern shown in Fig. 6(c) (obtained after annealing of the 0 K relaxed structure at 500 K for 200 ps), while the total dislocation length per unit interfacial area does not change.

In summary, we have studied the coherent and semi-coherent Al/α-Al$_2$O$_3$ interfaces with experimentally known orientation relationship $[\bar{1}10](111)_{\mathrm{Al}}\|[10\bar{1}0](0001)_{\mathrm{Al_2O_3}}$. Our atomistic simulations employed a "reference free" version of the modified embedded atom method (RF-MEAM) potential that is capable of adequately describe the charge transfer effects at the interface. The simulation results predict an interface dislocation structure with a network consisting of three sets of parallel dislocations, each with a pure edge character, surrounding hexagonal coherent regions and triangular stacking fault regions at the interface. The pattern formation can be rationalized in terms of a competition between the stacking fault energy and the dislocation interaction energy and has implications for dislocation dynamics models aimed at understanding the macroscopic mechanical behavior of the Al/α-Al$_2$O$_3$ composite heterostructures.

Methods

For our atomistic simulations, we employed a recently developed potential for the Al–O system[53], generated following a two-step construction method that is generally applicable to ionic systems. As non-electrostatic part of the potential we use a reference free version of the modified embedded atom method (RF-MEAM) potential that includes angular forces. For the electrostatic part we use the charge transfer ionic potential (CTIP) model proposed by Zhou *et al.* (here after referred to as ZWFN)[54]. The modified potential has been shown to achieve essential improvements over the ZWFN potential, derived by the incorporation of angular dependent forces and angular screening, as well as by the systematic fitting of the potential to a large energy database of different Al$_x$O$_y$ crystals, over a range of lattice constants and elastic deformations. The current potential yields more realistic atomic charges, crystal energies, lattice constants and correct ordering of phase stabilities for a range of Al–O systems. Moreover, O–O interactions as well as O interactions with a pure Al (111) and Al-terminated α-Al$_2$O$_3$ surfaces are realistically captured within this formulation.

For the coherent interfaces, aforementioned experimentally observed orientational relationship[17] with the Al-terminated interface was employed. The Al/α-Al$_2$O$_3$ interface was modeled in a slab geometry periodically repeating in the plane of the interface. The Al$_2$O$_3$ part of the interface contained six oxygen atomic layers and fourteen Al layers, and the metal part contains seven layers. A vacuum region of more than 35 Å was used between the periodically repeating slabs in the direction normal to the interface plane. The final interface structures are determined by relaxing all the internal coordinates until all the force components on the atoms were lower than 0.01 eV/Å. For the relaxation of the interface structures we have used an anneal-and-quench molecular dynamics (MD) formalism as described in the text, as opposed to the molecular statics.

To compare with the results of atomistic simulations obtained using our CTIP+RF–MEAM potential, the density functional theory (DFT)[55,56] computations for the coherent interface structures were performed using the Vienna *ab initio* simulation package (VASP)[57]. VASP uses a plane-wave basis set for the expansion of the single-particle Kohn-Sham wave functions. The projector-augmented wave (PAW) frozen-core potentials[58,59] were used to describe the electron-ion core interaction, and the quantum mechanical part of the electron-electron interactions was approximated using the Perdew-Burke-Ernzerhof (PBE) exchange-correlation functional[44]. Sampling of the irreducible wedge of the Brillouin zone is performed with a regular Monkhorst-Pack grid of special k-points[60]. To facilitate the numerical convergence associated with integrating the 0-K Fermi-Dirac distribution step-function, partial occupancies of the single-particle wave functions are introduced[61,62]. The electronic wave functions are expanded in plane waves up to a cut-off energy of 500 eV. A vacuum region of 15 Å was used to prevent any spurious unphysical interactions between the periodically repeating slabs in the direction normal to the interface plane. The final interface structures are determined by relaxing all the internal coordinates using the conjugate gradient method[63] until all the Hellmann-Feynman forces[64,65] were less than 0.01 V/Å.

The Frank-Bilby equation[45,48–50] used in our analysis is given as follows:

$$\sum_{l} \frac{\vec{b}_l sin\gamma^l}{L^l} = D_{rc}\hat{p}. \qquad (5)$$

Here, index l runs over all the unique sets of dislocation lines present at the interface, each with Burgers vector $\vec{b}_l$ and separation length L^l between the parallel lines within a given set. γ^l denotes the angle between a dislocation line direction ξ^l and the probe unit vector $\hat{p}$, measured in the anti-clockwise direction. D_{rc} represents a deformation matrix that maps a unit vector in the coherent reference configuration onto the interface structure containing dislocations.

1. Kröger, F. A. Electrical properties of α-Al$_2$O$_3$, *Structure and properties of MgO and Al$_2$O$_3$ ceramics*, Kingery, W. D. (ed.), 1–15 (American Ceramic Society, USA, 1984).
2. Chatain, D., Coudurier, L. & Eustathopoulos, N. Wetting and interfacial bonding in ionocovalent oxide-liquid metal systems. *Rev. Phys. Appl.* **23**, 1055–1064 (1988).
3. French, R. H. & Heuer, A. H. International Workshop on the Science of Alumina. *J. Am. Ceram. Soc.*, **77**, 292–292 (1994).
4. Bortz, M. L. *et al.* Temperature dependence of the electronic structure of oxides: MgO, MgAl—2O$_4$ and Al$_2$O$_3$. *Phys. Scr.* **41**, 537–541 (1990).

5. Amano, H., Sawaki, N., Akasaki, I. & Toyoda, Y. Metalorganic vapor phase epitaxial growth of a high quality GaN film using an AlN buffer layer. *Appl. Phys. Lett.* **48**, 353–355 (1986).
6. Di Felice, R. & Northrup, J. E. Theory of the clean and hydrogenated $Al_2O_3(0001)$-(1×1) surfaces. *Appl. Phys. Lett.* **73**, 936–938 (1998).
7. Freund, H.-J., Kuhlenbeck, H. & Staemmler, V. Oxide surfaces. *Rep. Prog. Phys.* **59**, 283–347 (1996).
8. Ksiazek, M., Sobczak, N., Mikulowski, B., Radziwill, W. & Surowiak, I. Wetting and bonding strength in Al/Al_2O_3 system. *Mater. Sci. Eng. A* **324**, 162–167 (2002).
9. Gupta, V., Argon, A. S. & Cornie, J. A. Interfaces with controlled toughness as mechanical fuses to isolate fibres from damage. *J. Mater. Sci.* **24**, 2031–2040 (1989).
10. Fu, Q. & Wagner, T. Interaction of nanostructured metal overlayers with oxide surfaces. *Surf. Sci. Rep.* **62**, 431–498 (2007).
11. Yang, K. S., Choi, J. S., Lee, S. H. & Chung, J. S. Development of Al/Al_2O_3-coated wire-mesh honeycombs for catalytic combustion of volatile organic compounds in air. *Ind. Eng. Chem. Res.* **43**, 907–912 (2004).
12. Champion, J. A., Keene, B. J. & Sillwood, J. M. J. Wetting of aluminium oxide by molten aluminium and other metals. *Mater. Sci.* **4**, 39–49 (1969).
13. Laurent, V., Chatain, D., Chatillon, C. & Eustathopoulos, N. Wettability of monocrystalline alumina by aluminium between its melting point and 1273 K. *Acta. Mater.* **36**, 1797–1803 (1988).
14. Vermeersch, M., Sporken, R., Lambin, P. & Caudano, R. The $Al/Al2O_3$ interface formation as studied by electron spectroscopies. *Surf. Sci.* **235**, 5–14 (1990).
15. Vermeersch, M., Malengreau, F., Sporken, R. & Caudano, R. The aluminium/sapphire interface formation at high temperature: an AES and LEED study. *Surf. Sci.* **323**, 175–187 (1995).
16. Zhou, X. B. & De Hosson, J. M. Wetting kinetics of liquid aluminium on an Al_2O_3 surface. *J. Mater. Sci.* **30**, 3571–3575 (1995).
17. Medlin, D. L., McCarty, K. F., Hwang, R. Q., Guthrie, S. E. & Baskes, M. I. Orientation relationships in heteroepitaxial aluminum films on sapphire. *Thin Solid Films* **299**, 110–114 (1997).
18. Levi, G. & Kaplan, W. D. Oxygen induced interfacial phenomena during wetting of alumina by liquid aluminium. *Acta Mater.* **50**, 75–88 (2002).
19. Shen, P., Fujii, H., Matsumoto, T. & Nogi, K. The influence of surface structure on wetting of α-Al_2O_3 by aluminum in a reduced atmosphere. *Acta Mater.* **51**, 4897–4906 (2003).
20. Lazzari, R. & Jupille, J. Wetting and interfacial chemistry of metallic films on the hydroxylated α-$Al_2O_3(0001)$ surface. *Phys. Rev. B* **71**, 045409 (2005).
21. Fu, Q., Wagner, T. & Rühle, M. Hydroxylated α-Al_2O_3 (0001) surfaces and metal/α-Al_2O_3 (0001) interfaces. *Surf. Sci.* **600**, 4870–4877 (2006).
22. Sangghaleh, A. & Halali, M. An investigation on the wetting of polycrystalline alumina by aluminium. *J. Mater. Process. Technol.* **197**, 156–160 (2008).
23. Anderson, A. B., Mehandru, S. P. & Smialek, J. L. Dopant Effect of Yttrium and the Growth and Adherence of Alumina on Nickel-Aluminum Alloys. *J. Electrochem. Soc.* **132**, 1695–1701 (1985).
24. Angelo, J. E. & Baskes, M. I. Interfacial studies using the EAM and MEAM. *Interface Sci.* **4**, 47–63 (1996).
25. Zhang, W. & Smith, J. R. Nonstoichiometric interfaces and Al_2O_3 adhesion with Al and Ag. *Phys. Rev. Lett.* **85**, 3225–3228 (2000).
26. Batyrev, I. G. & Kleinman, L. In-plane relaxation of Cu (111) and Al (111)/α-$Al_2O_3(0001)$ interfaces. *Phys. Rev. B* **64**, 033410 (2001).
27. Wang, X.-G., Smith, J. R. & Evans, A. Fundamental Influence of C on Adhesion of the Al_2O_3/Al Interface. *Phys. Rev. Lett.* **89**, 286102 (2002).
28. Siegel, D. J., Hector Jr, L. G. & Adams, J. B. Adhesion, atomic structure, and bonding at the Al (111)/α-$Al_2O_3(0001)$ interface: A first principles study. *Phys. Rev. B* **65**, 085415 (2002).
29. Siegel, D. J., Hector, L. G. & Adams, J. B. Ab initio study of Al-ceramic interfacial adhesion. *Phys. Rev. B* **67**, 092105 (2003).
30. Zhang, Q. *et al.* Adhesion and nonwetting-wetting transition in the Al/α-Al_2O_3 interface. *Phys. Rev. B* **69**, 045423 (2004).
31. Kang, J. *et al.* Atomically Abrupt Liquid-Oxide Interface Stabilized by Self-Regulated Interfacial Defects: The Case of Al/Al_2O_3 Interfaces. *Phys. Rev. Lett.* **108**, 226105 (2012).
32. Streitz, F. H. & Mintmire, J. W. Electrostatic potentials for metal-oxide surfaces and interfaces. *Phys. Rev. B* **50**, 11996–12003 (1994).
33. Streitz, F. H. & Mintmire, J. W. Metal/oxide interfaces: An electrostatics-based model. *Compos. Interfaces* **2**, 473–484 (1994).
34. Saiz, E., Cannon, R. M. & Tomsia, A. O. Energetics and Atomic transport at liquid-metal/Al_2O_3 interfaces. *Acta Mater.* **47**, 4209–4220 (1999).
35. Merlin, V. & Eustathopoulos, N. Wetting and adhesion of Ni-Al alloys on α-Al_2O_3 single crystals. *J. Mater. Sci.* **30**, 3619–3624 (1995).
36. Evans, A. G., Mumm, D. R., Hutchinson, J. W., Meier, G. H. & Pettit, F. S. Mechanisms controlling the durability of thermal barrier coatings. *Prog. Mater. Sci.* **46**, 505–553 (2001).
37. Oh, S. H. *et al.* Oscillatory mass transport in vapor-liquid-solid growth of sapphire nanowires. *Science* **330**, 489–493 (2010).
38. Streitz, F. H. & Mintmire, J. W. Energetics of aluminum vacancies in gamma alumina. *Phys. Rev. B* **60**, 773–777 (1999).
39. Duin, A. C. T., van, Dasgupta, S., Lorant, F. & Goddard III, W. A. J. ReaxFF: A Reactive Force Field for Hydrocarbons. *Phys. Chem. A* **105**, 9396–9409 (2001).
40. Alpas, A. T., Embury, J. D., Hardwick, D. A. & Springer, R. W. The mechanical properties of laminated microscale composites of $A1/Al_2O_3$. *J. Mat. Sci.* **25**, 1603–1609 (1990).
41. Pilania, G., Zhu, H. & Ramprasad, R. *Applications of Modern Density Functional Theory to Surfaces and Interfaces.* In A Matter of Density: Exploring the Electron Density Concept in the Chemical, Biological, and Materials Sciences, ed. Sukumar, pp 271–312 (John Wiley & Sons, Inc., New Jersey, 2012).
42. Alankar, A., Field, D. P. & Zbib, H. M. Explicit incorporation of cross-slip in a dislocation density-based crystal plasticity model. *Phil. Mag.* **92**, 3084–3100 (2012).
43. Uchic, M. D., Shade, P. A. & Dimiduk, D. Plasticity of micrometer-scale single crystals in compression. *Annu. Rev. Mater. Res.* **39**, 361–386 (2009).
44. Perdew, J. P., Burke, K. & Ernzerhof, M. Generalized gradient approximation made simple. *Phys. Rev. Lett.* **77**, 3865–3868 (1996).
45. Hirth, J. P., Pond, R. C., Hoagland, R. G., Liu, X.-Y. & Wang, J. Interface defects, reference spaces and the Frank-Bilby equation. *Prog. Mater. Sci.* **58**, 749–823 (2013).
46. Wang, J., Hoagland, R. G. & Misra, A. Atomistic modeling of the interface of glide dislocations with "weak" interfaces. *Acta Mater.* **56**, 5685–5693 (2008).
47. Liu, X.-Y., Hoagland, R. G., Wang, J., Germann, T. C. & Misra, A. The influence of dilute heats of mixing on the atomic structures, defect energetics and mechanical properties of fcc-bcc interfaces. *Acta Mater.* **58**, 4549–4557 (2010).
48. Frank, F. C. Martensite. *Acta Met.* **1**, 15–19 (1953).
49. Bilby, B. A. *Bristol Conference Report on Defects in Crystalline Solids* (The Physical Society, London 1955, p. 124).
50. Bilby, B. A., Bullough, R. & Smith, E. Continuous distributions of dislocations: a new application of the methods of non-Riemannian geometry. *Proc. Roy. Soc. (London)* **A231**, 263–273 (1955).
51. Shao, S., Wang, J., Misra, A. & Hoagland, R. G. Spiral Patterns of Dislocations at Nodes in (111) Semi-coherent FCC Interfaces. *Sci. Rep.* **3**, 2448; DOI:10.1038/srep02448 (2013).
52. Ernst, F. Metal-oxide interfaces. *Mater. Sci. Eng.* **R14**, 97–156 (1995).
53. Lazić, I. & Thijsse, B. J. An improved molecular dynamics potential for the Al-O system. *Comp. Mat. Sci.* **53**, 483–492 (2012).
54. Zhou, X. W., Wadley, H. N. G., Filhol, J. S. & Neurock, M. N. Modified charge transfer-embedded atom method potential for metal/metal oxide systems. *Phys. Rev. B* **69**, 035402 (2004).
55. Hohenberg, P. & Kohn, W. Inhomogeneous electron gas. *Phys. Rev.* **136**, B864–B871 (1964).
56. Kohn, W. & Sham, L. J. Self-consistent equations including exchange and correlation effects. *Phys. Rev.* **140**, A1133–A1138 (1965).
57. Kresse, G. & Furthmüller, J. Efficient iterative schemes for ab initio total-energy calculations using a plane-wave basis set. *Phys. Rev. B* **54**, 11169–11186 (1996).
58. Blöchl, P. E. Projector augmented-wave method. *Phys. Rev. B* **50**, 17953–17979 (1994).
59. Kresse, G. & Joubert, D. From ultrasoft pseudopotentials to the projector augmented-wave method. *Phys. Rev. B* **59**, 1758–1775 (1999).
60. Monkhorst, H. J. & Pack, J. D. Special points for Brillouin-zone integrations. *Phys. Rev. B* **13**, 5188–5192 (1976).
61. Mermin, N. D. Thermal properties of the inhomogeneous electron gas. *Phys. Rev.* **137**, A1441–A1443 (1965).
62. Fu, C.-L. & Ho, K.-M. First-principles calculation of the equilibrium ground-state properties of transition metals: Applications to Nb and Mo. *Phys. Rev. B* **28**, 5480–5486 (1983).
63. Press, W. H., Teukolsky, S. A., Vetterling, W. T. & Flannery, B. P. *Numerical Recipes in Fortran 90: The Art of Parallel Scientific Computing,* 2nd ed. (Cambridge University Press, Cambridge, England, 1996).
64. Hellmann, H. *Einführung in die Quantumchemie* (Deuticke, Leipzig, 1937).
65. Feynman, R. P. Forces in molecules. *Phys. Rev.* **56**, 340–343 (1939).

Acknowledgments

This work was supported by the Los Alamos National Laboratory (LANL) Directed Research and Development Program (20120053ER) and the US Department of Energy, Office of Science, Office of Basic Energy Sciences. LANL is operated by Los Alamos National Security, LLC, for the National Nuclear Security Administration of the U.S. Department of Energy under Contract No. DE-AC52-06NA25396. Helpful discussions with Terry Mitchell and Shuai Shao are gratefully acknowledged.

Author contributions

The project was conceived by X.Y.L. and R.G.H. The theoretical computations were performed by G.P.; B.J.T. and I.L. provided the CTIP-RMEAM potential used to carryout the simulations. All the authors participated in writing the manuscript and S.M.V. reviewed the manuscript.

Additional information

Competing financial interests: The authors declare no competing financial interests.

How to cite this article: Pilania, G. *et al*. Revisiting the Al/Al_2O_3 Interface: Coherent Interfaces and Misfit Accommodation. *Sci. Rep.* **4**, 4485; DOI:10.1038/srep04485 (2014).

This work is licensed under a Creative Commons Attribution-NonCommercial-ShareAlike 3.0 Unported license. To view a copy of this license, visit http://creativecommons.org/licenses/by-nc-sa/3.0